

ARTICLE

DOI: 10.1038/s41467-017-02676-w

OPEN

Au@Nb@H_xK_{1-x}NbO₃ nanopeapods with near-infrared active plasmonic hot-electron injection for water splitting

Ying-Chu Chen¹, Yu-Kuei Hsu², Radian Popescu³, Dagmar Gerthsen³, Yan-Gu Lin⁴ & Claus Feldmann¹

Full-spectrum utilization of diffusive solar energy by a photocatalyst for environmental remediation and fuel generation has long been pursued. In contrast to tremendous efforts in the UV-to-VIS light regime of the solar spectrum, the NIR and IR areas have been barely addressed although they represent about 50% of the solar flux. Here we put forward a biomimetic photocatalyst blueprint that emulates the growth pattern of a natural plant—a peapod—to address this issue. This design is exemplified via unidirectionally seeding core-shell Au@Nb nanoparticles in the cavity of semiconducting H_xK_{1-x}NbO₃ nanoscrolls. The biomimicry of this nanopeapod (NPP) configuration promotes near-field plasmon–plasmon coupling between bimetallic Au@Nb nanoantennas (the peas), endowing the UV-active H_xK_{1-x}NbO₃ semiconductor (the pods) with strong VIS and NIR light harvesting abilities. Moreover, the characteristic 3D metal–semiconductor junction of the Au@Nb@H_xK_{1-x}NbO₃ NPPs favors the transfer of plasmonic hot carriers to trigger dye photodegradation and water photoelectrolysis as proofs-of-concept. Such broadband solar spectral response renders the Au@Nb@H_xK_{1-x}NbO₃ NPPs highly promising for widespread photoactive devices.

¹Institut für Anorganische Chemie, Karlsruhe Institute of Technology (KIT), Engesserstraße 15, Karlsruhe D-76131, Germany. ²Department of Opto-Electronic Engineering, National Dong Hwa University, Hualien 97401, Taiwan. ³Laboratorium für Elektronenmikroskopie, Karlsruhe Institute of Technology (KIT), Engesserstraße 7, Karlsruhe D-76131, Germany. ⁴National Synchrotron Radiation Research Center, Hsinchu 30076, Taiwan. Ying-Chu Chen and Yu-Kuei Hsu contributed equally to this work. Correspondence and requests for materials should be addressed to C.F. (email: claus.feldmann@kit.edu)

For millennia, nature routinely has fed humanity with useful energy in either food supplies or carbon-based fuels by solar-to-chemical conversion, namely photosynthesis using sunlight^{1–4}. In particular, these carbohydrates are produced from water and carbon dioxide. The sustainability and environmental benignity in the context of photosynthesis have inspired scientists and engineers to emulate so-called artificial photosynthesis or photocatalysis using man-made materials^{5–12}. One of the major endeavors in the field addresses the sunlight-harvesting ability of the photocatalyst, preferentially ranging from ultraviolet (UV) to visible (VIS) light—accounting for nearly 50% of the solar spectrum—to photogenerate electron/hole pairs (e^-/h^+) for fuel production^{13–17}. Although near-infrared (NIR) light is responsible for an additional 50% of the solar flux, quite to our surprise, further exploitation on its charge-carrier-generation efficacy is currently in its infancy^{18–21}. In the light of its enormous percentage in sunlight, charge-carrier generation in the NIR spectral region is of obvious significance.

To this end, coupling of a photocatalyst with plasmonic nanoantennas stands out since the size and shape of metallic nanostructures can be readily used to tailor the light-harvesting ability^{7,22,23}. Knight et al.²⁴ demonstrated for the first time that an array of rod-shaped Au nanoantennas allows NIR light to trigger a current response on a silicon-based photodiode, even though the wavelength (1250–1600 nm) is well below the semiconductor band gap. The NIR-promoted e^-/h^+ pairs arise exclusively from non-radiative damping of surface plasmons on Au. More importantly, they become accessible to a Si diode with the aid of a Schottky junction at the metal-to-semiconductor interface, in which the energy barrier is much smaller for those energetic or hot electrons than the band gap of Si. The significance of these results lies in corroborating the propensity of NIR light to induce useful energetic e^-/h^+ pairs in photoactive devices.

Recently, those hot charge carriers prompted by NIR-excited plasmons were reported not only to generate electricity^{24–27} but also to support chemical fuel generation^{20,21,28}, thereby addressing a paradigm in photocatalysis. Hence, Mubeen et al.²⁸ reported on the evidence of hydrogen (H_2) gas evolution on a photoexcited dense Au nanorod (NR) array that was sprinkled atop with a bifunctional TiO_2 semiconductor and laterally with a cobalt-based oxygen-evolution catalyst (Co-OEC) in the presence of a sacrificial agent. Furthermore, Zheng et al.²¹ introduced an alternative of strewing the tips of Au NRs merely with Pt in lieu of TiO_2 and Co-OEC. The dual functionality of Pt, on the one hand, includes serving as an electron sink to prevent hot electrons to drift back to the Au NRs. This is also the asset and function of a Schottky junction. Moreover, the catalytic effect of Pt allows H_2 generation in the presence of a photohole scavenger. These results validate the persistence of energetic electrons in producing H_2 upon photoexcitation of Au NR with visible-NIR light radiation. However, the direct exposure of the plasmonic metals to the electrolyte can result in undesirable corrosion and/or dissolution of the Au NR during reaction^{22,23,29}. As an alternative, we here suggest a metal-semiconductor composite structure with the plasmonic nanoantennas embedded in the semiconductor, emerging as a breakthrough to retrieve the aforementioned depleted photoactivity. Even more important, the concomitant 3D heterojunction of such metal-semiconductor composite can also support hot-electron injection due to the substantially increased metal-to-semiconductor interface^{27,30}.

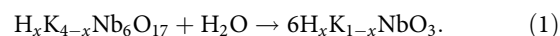
In this contribution, we implanted Au@Nb core-shell nanoparticles (CS-NP) into the cavity of tubular protonated metaniobate ($H_xK_{1-x}NbO_3$) nanoscrolls (NSs). In particular, this infiltration emulates the design of a natural plant, namely, peapods. Thus, Au@Nb CS-NPs are unidirectionally deposited yet

mutually isolated with a break of few nanometers in between. In addition to the passivation against photocorrosion and the enhanced Schottky junction area, the biomimicry of this peapod design endow the Au@Nb@ $H_xK_{1-x}NbO_3$ nanopeapod (NPP) photocatalyst with an exceptional broadband photoabsorption ability that eminently matches with the solar spectrum. In particular, the outmost $H_xK_{1-x}NbO_3$ semiconductor NS (the pod) is responsible for UV light absorption, whereas the inner Au@Nb CS-NPs (the peas) account for visible light absorption via surface plasmon resonance (SPR). Most significantly, this nanopeapod design gives rise to a strong near-field interantenna coupling that additionally creates the excellent photoresponse of Au@Nb@ $H_xK_{1-x}NbO_3$ NPPs to NIR light. To the best of our knowledge, this peculiar NPP design is the first alternative pattern—in addition to the geometry and size—to effectively expand the resonant plasmon wavelength of Au nanoantennas over the full solar spectrum. The resulting effective NIR-induced dye decolorization and water cleavage in the absence of an irreversible whole scavenger substantiate the relevance and potential of the peapod-structured photocatalyst.

Results

Synthesis and characterization of Au@Nb@ $H_xK_{1-x}NbO_3$ nanopeapods. The peapod design is foremost characterized by the tubular morphology of the semiconductor. Moreover, the passivation of the encapsulated plasmonic metal is a most relevant aspect to avoid its dissolution due to photocorrosion processes. To this regard, oxide-based materials known for high stability—particularly, TiO_2 , $\alpha-Fe_2O_3$ or niobates—are promising semiconductors that were already shown to form tubular nanostructures^{31–33}. Hereof, $H_xK_{1-x}NbO_3$ is favored due to its delicate band-edge position straddling most redox reactions of interest, and due to the d -orbital nature of its conduction band rendering abundant density of states (DOSSs) for a rapid electron uptake^{34,35}.

Preparing $H_xK_{1-x}NbO_3$ directly from either $HNbO_3$ or $KNbO_3$ in an anisotropic tubular shape, however, is not straightforward as both have a cubic structure^{36,37}. Such cubic symmetry typically leads to the formation of an isotropic crystallite growth most often resulting in cubes or octahedra^{6,36}. To fabricate tubular $H_xK_{1-x}NbO_3$ either by protonating of $KNbO_3$ or by exchange of protons (H^+) in $HNbO_3$ by potassium (K^+) ions seems highly unlikely. Here we have addressed this issue by using the orthorhombic potassium hexaniobate ($K_4Nb_6O_{17}$) as the starting material, which already has a lamellar structure and which is thus ideal as a template^{38–40}. Hence, the synthesis started with the $K_4Nb_6O_{17}$ template that was subsequently subjected to a cascade of reactions mainly including an interlamellar ion exchange (i.e., $H_xK_{4-x}Nb_6O_{17}$) to degenerate its structural integrity followed by an exfoliation process of individual lamella by bulky tetrabutylammonium (TBA^+) ions (Fig. 1a–c). The resulting isolated molecular sheets then undergo automatic curling due to an intrinsic lattice asymmetry inside each lamella and finally forms structured tubular NSs³⁸. Hereof, the last two steps using a strongly hydrated tetrabutylammonium hydroxide and an organic media are the key to promote the desired phase transformation, in which the dissociation of coordinated water molecules from TBA^+ was retarded that otherwise promote the exfoliated $H_xK_{4-x}Nb_6O_{17}$ lamella to undergo hydrolysis at high temperature according to Equation (1)^{36,40}.



It is worth mentioning that the $H_xK_{4-x}Nb_6O_{17}$ sheets consist of a central layer of $[NbO_6]$ octahedra shearing corners in the [100] direction and alternating edges and corners in the [001] direction

(Fig. 1c)^{36,37}. Such corner-shearing $[\text{NbO}_6]$ octahedra are also an inherent structural feature of the $\text{H}_x\text{K}_{1-x}\text{NbO}_3$ perovskite (Fig. 1d) serving as a backbone and facilitating the phase transformation. Such templated crystallization can be regarded as topotactic reaction, in which the template is subjected to a phase transition without sacrificing its morphology (Fig. 1e). Selected area electron diffraction (SAED) patterns (Fig. 1f, top) and azimuthally averaged SAED patterns (Fig. 1f, bottom) of an $\text{Au@Nb@H}_x\text{K}_{1-x}\text{NbO}_3$ NPP ensemble show (002), (112), and (004) reflections belonging to the $\text{H}_x\text{K}_{1-x}\text{NbO}_3$ perovskite (space group $Im-3$, $a=7.65$ Å). In addition, reflections of pure Au (face-centered-cubic structure, space group $Fm-3m$, $a=4.08$ Å) and Nb (body-centered cubic structure, space group $Im-3m$, $a=3.32$ Å) are visible. Geometric features of the finally formed $\text{H}_x\text{K}_{1-x}\text{NbO}_3$ NSs are delineated by transmission electron microscopy (TEM) with an orifice diameter of about $d=20$ nm and an outer scroll diameter in a range of $D=35-70$ nm (Fig. 1e), while the length of the NSs lies between 0.1 and 1.0 μm (Fig. 1g). The photoabsorption, which is another crucial property with regard to photocatalysis application, was characterized through diffuse reflectance spectroscopy (DRS).

Hence, a featured absorption edge at 390 nm (Fig. 1h, inset) results in a band gap of 3.07 eV (Fig. 1h) for the $\text{H}_x\text{K}_{1-x}\text{NbO}_3$ NSs, which is in good agreement with the values reported in the literature^{41,42}. A slight decrement of the band gap is presumably related to weakened Nb–O–Nb bonds originating from the curling of the niobate layers to form the NSs⁴³.

To date, there is a variety of technologies for fabricating 1D Au peapodded nanostructures, including vapor–liquid–solid (VLS) growth and atomic layer deposition (ALD)^{44–46}. However, the Rayleigh perturbation at the tempering step in those approaches generally generates NPPs with an interparticle spacing (d_{gap}) of nearly 100 nm which fairly exceeds the diameter of the Au particles (d_{Au}) and which leads to a ratio of interdistance over diameter ($d_{\text{gap}}/d_{\text{Au}} > 1$). Such giant spacing hinders the surface plasmon polaritons (SPPs) on photoexcited Au NPs from electric near-field coupling^{47–50}. As a consequence, a waning photoresponse at excitation wavelengths remote from the characteristic SPR was reported^{44–46}. In order to retrieve the fading plasmon coupling, this article tackles this challenge by taking a dissolved Au precursor in place of a solid Au catalyst to exclude the

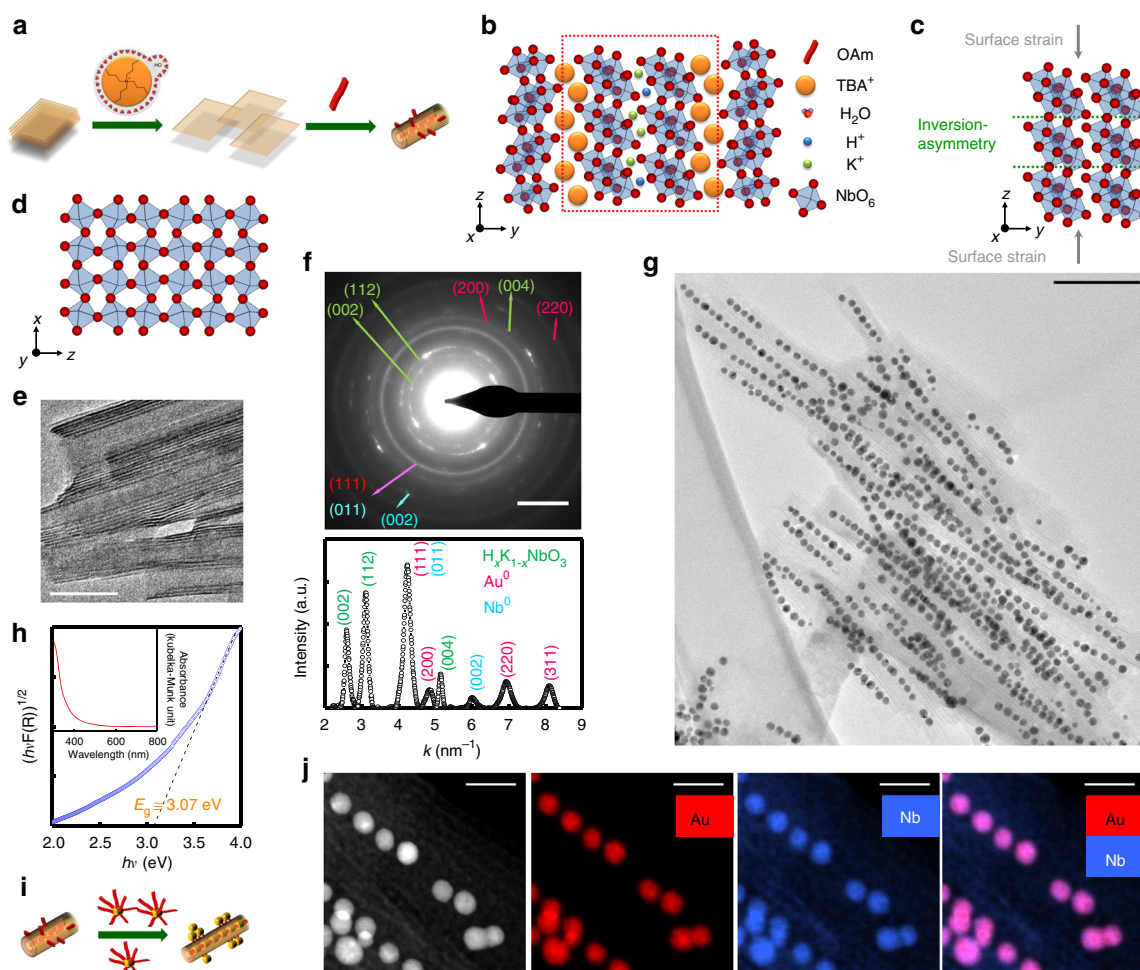


Fig. 1 Stepwise formation and characterization of $\text{Au@Nb@H}_x\text{K}_{1-x}\text{NbO}_3$ NPPs. **a** Schematic and **b, c** crystallographic illustrations of the morphological evolution of templated $\text{H}_x\text{K}_{1-x}\text{Nb}_6\text{O}_{17}$ crystallites to lamellar and tubular colloids. **d** Crystal structure of cubic HNbO_3 perovskite. **e** TEM image (scale bar: 70 nm) of tubular $\text{H}_x\text{K}_{1-x}\text{NbO}_3$ NSs, in which the hollow cavity functions as the host to breed the Au@Nb CS-NPs. **f** SAED pattern (top, scale bar: 3 nm), corresponding azimuthally averaged SAED pattern (bottom) and **g** TEM image (scale bar: 100 nm) of the $\text{Au@Nb@H}_x\text{K}_{1-x}\text{NbO}_3$ NPPs. **h** Absorption spectrum (inset) and derived Tauc plot of the $\text{H}_x\text{K}_{1-x}\text{NbO}_3$ NSs. **i** Schematic highlights of the biomimicry of the $\text{Au@Nb@H}_x\text{K}_{1-x}\text{NbO}_3$ NPPs, wherein the Au@Nb CS-NPs as the “peas” are unidirectionally loaded into the tubular cavity of nanoscale $\text{H}_x\text{K}_{1-x}\text{NbO}_3$ as the “pods”. **j** HAADF-STEM image and EDXS elemental maps (scale bars: 20 nm) of the Au (red), Nb (blue), and combined Au/Nb distribution prove the structure of the $\text{Au@Nb@H}_x\text{K}_{1-x}\text{NbO}_3$ NPPs, in which the Au@Nb CS-NPs (lilac) are unidirectionally located inside the $\text{H}_x\text{K}_{1-x}\text{NbO}_3$ NSs (blue). Abbreviations used: OAm, oleylamine; TBA⁺, tetrabutylammonium cation; NS, nanoscroll; CS-NPs, core-shell nanoparticles; NPP, nanopod

necessity of any thermal treatment⁵¹. Moreover, such solution-processed Au precursors can readily be capillary engulfed into the cavity of the preformed $H_xK_{1-x}NbO_3$ NSs. Afterwards, the employment of a reducing agent (i.e., oleyamine) allows the Au NPs to seed directly inside the semiconductor NSs (Fig. 1i). Figure 1g, j summarize TEM, high-angle annular dark-field scanning TEM (HAADF-STEM) and energy dispersive X-ray spectroscopy (EDXS) results that clearly depict the morphology and the Au and Nb distribution of the as-prepared NPPs. The TEM images (Fig. 1g, j) highlight the uniformity and filling efficacy while the unidirectionally aligned bright spots in HAADF-STEM images and the distinct elemental contrast in EDXS mappings (Fig. 1j) point to the arrangement of the Au NPs and the niobate NSs in the $Au@H_xK_{1-x}NbO_3$ NPPs, respectively.

Characterization of the Au@Nb core-shell nanoparticles. The high yield of the $Au@H_xK_{1-x}NbO_3$ NPPs distinctly indicates a strong contrast between Au nucleation rates outside and inside the niobate NSs. This discrepancy originates from the presence of oleyamine (OAm) at the earliest scroll formation stage (Fig. 1a)^{40,51}. Hence, OAm can saturate the cavity of the NSs and accelerates the

growth rate of inner Au nanopeas. Surprisingly, EDXS (Fig. 1j) of those inner Au nanopeas reveals an exceptional effect of this preliminary treatment. Namely, OAm intercepts the niobium (Nb^{5+}) leakage from $H_xK_{4-x}Nb_6O_{17}$ during the phase transition to the final $H_xK_{1-x}NbO_3$ that contains a lower stoichiometric content of Nb³⁶. The excess Nb^{5+} in turn is deposited as Nb^0 atop the nucleated Au NPs (element maps in Fig. 1j); concentration profiles across single NPs in Fig. 2a–c) via underpotential deposition (UPD), resulting in the exceptional $Au@Nb@H_xK_{1-x}NbO_3$ multi-core-shell peapod structure (Supplementary Figs 1–3, see Supplementary Methods and Supplementary Note 1 for details). $Au@Nb$ CS-NPs with different Nb distributions are observed by high-resolution (HR) TEM (Fig. 2d–f) and the corresponding Nb-line profiles across single CS-NPs (Fig. 2a–c). Figure 2d shows a CS-NP with single-crystalline structure and a continuous Nb shell with a thickness of 1–2 nm (Fig. 2a). We note that $H_xK_{1-x}NbO_3$ NSs cannot be seen in the HRTEM images due to their low contrast compared to the CS-NP contrast, but they can be well recognized in TEM overview images (Fig. 2g).

CS-NPs within $H_xK_{1-x}NbO_3$ NSs (red frame in Fig. 2g) are typically covered by a continuous Nb shell as demonstrated by Fig. 2a, d. The formation of a pure Nb shell (instead of Nb oxide)

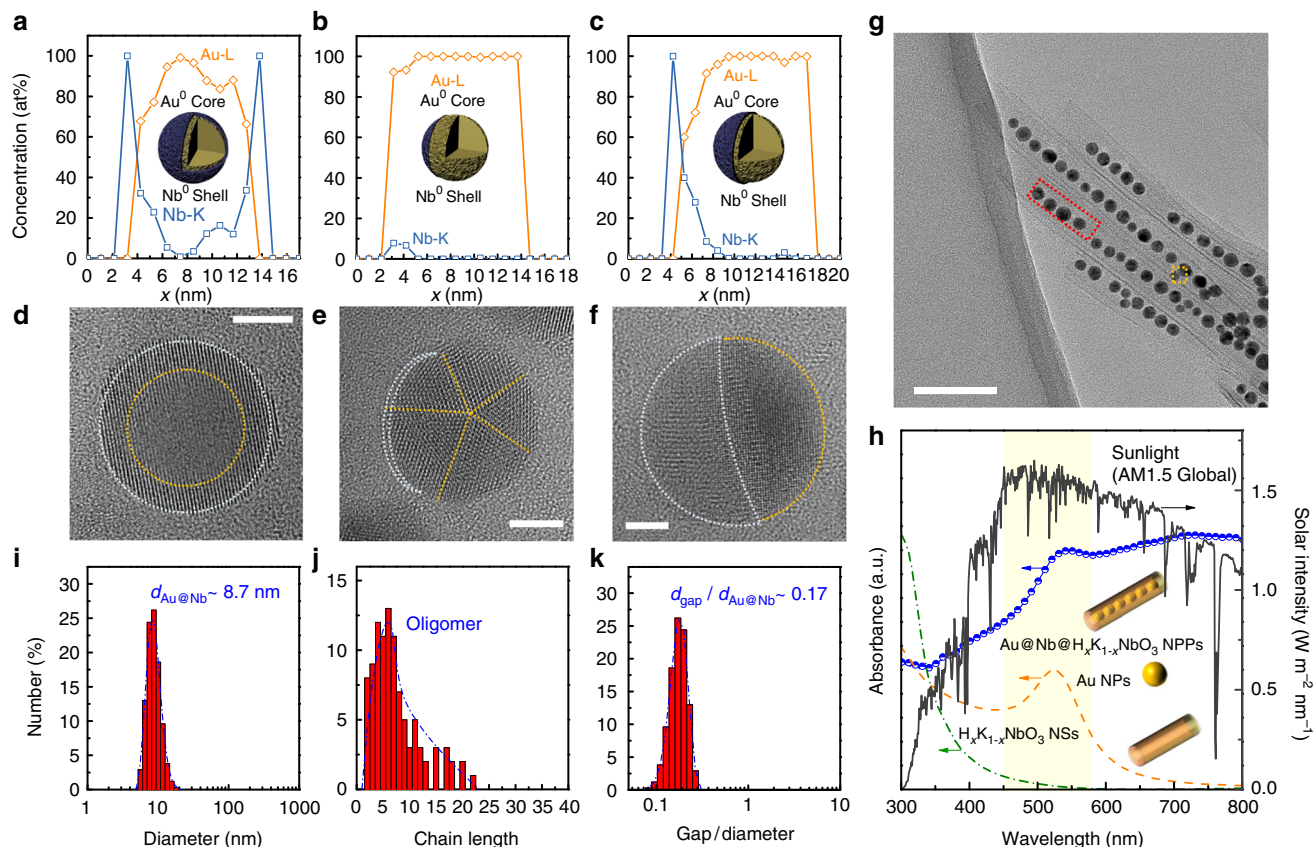


Fig. 2 CS-NP configuration and configuration-dependent surface plasmon resonances of the $Au@Nb@H_xK_{1-x}NbO_3$ NPPs. **a–c** EDXS line profiles (element contributions from the $H_xK_{1-x}NbO_3$ NSs were subtracted) and **d–f** corresponding HRTEM images reveal the CS-NP configuration of the $Au@Nb@H_xK_{1-x}NbO_3$ NPPs. Orange and white dashed lines in the HRTEM images delineate core and shell boundaries (lines are guide to the eye) of single-crystalline $Au@Nb$ CS-NPs with a continuous Nb shell (**a, d**) (scale bar: 4 nm); multiply twinned Au NPs with thin incomplete Nb shells (**b, e**) (scale bar: 3 nm); $Au@Nb$ CS-NPs with a partial Nb shell (**c, f**) (scale bar: 2 nm). **g** TEM overview image (scale bar: 50 nm) of the $Au@Nb@H_xK_{1-x}NbO_3$ NPPs showing the $Au@Nb$ CS-NPs located within (red frame) and on (orange frame) the $H_xK_{1-x}NbO_3$ NSs. **h** Absorption spectrum of the $Au@Nb@H_xK_{1-x}NbO_3$ NPPs (half-filled circles). AM 1.5G solar spectrum (solid line), naked Au NPs (dashed line), and hollow $H_xK_{1-x}NbO_3$ NSs counterparts (dash-dotted line) are plotted also for comparison. **i–k** Pattern features of the $Au@Nb$ CS-NPs with **i** particle size, **j** length of continuous CS-NP chains (in number of CS-NPs per chain) and **k** interparticle distance in units of $Au@Nb$ particle size, respectively. Experimental data determined from different TEM images and fits of these data (blue dashed lines). Abbreviations used: $d_{Au@Nb}$, diameter of bimetallic $Au@Nb$ nanoparticle; d_{gap} , interparticle distance between adjacent $Au@Nb$ nanoparticles of the $Au@Nb@H_xK_{1-x}NbO_3$ NPP; NSs, nanoscrolls; NPs, nanoparticles; NPPs, nanopeapods

is further supported by its structure, which corresponds to bulk cubic Nb (Supplementary Fig. 4). Inhomogeneous Nb distributions are found for CS-NPs at the outer surface of the $H_xK_{1-x}NbO_3$ NSs. For example, the CS-NP in Fig. 2e is only partially covered by a Nb shell (Fig. 2b). The Au core of this NP exhibits a multiply twinned structure with a decahedral shape along its fivefold symmetry axis (Supplementary Fig. 5). The CS-NP in Fig. 2c, f forms a Nb bridge at the interface toward the niobate NSs. The position of this CS-NP is marked by an orange frame in Fig. 2g. The Bragg reflections of the CS-NPs are also present in the SAED pattern (Fig. 1f), where Au (200), (220), and (311) diffraction rings with a uniform intensity support the conclusions from the HRTEM analysis. The intensity of the Nb reflections is in general weak due to the small Nb amount contained in the CS-NPs but the Nb (002) reflection can be clearly recognized in the azimuthally averaged SAED pattern (Fig. 1f, bottom). These analyses show exemplary features of bimetallic CS-NPs prepared by an UPD process, which refers to the deposition of a metal film with the thickness up to few atomic layers on a foreign metal substrate at a potential much more positive than that for the deposition on the same metal surface⁵². Accordingly, UPD is the most likely mechanism for the formation of metallic Nb (standard reduction potential -0.64 V vs. SHE) by OAm in the presence of Au NPs.

Broadband light harvesting ability. One of the important merits of the unique Au@Nb CS-NP formation is that the Nb shell can superimpose its characteristic SPR absorption upon that of the Au core to modulate the optical properties of the Au@Nb CS-NPs⁵³. As a consequence, the Au@Nb@ $H_xK_{1-x}NbO_3$ NPPs produce an absorption spectrum (Fig. 2h), exhibiting a somewhat flatter nature at wavelengths beyond 400 nm (featured SPR absorption of Nb) yet below 530 nm (featured SPR wavelength of Au)^{22,23,54}. Intriguingly, a similar scenario is also observed at wavelengths beyond the SPR frequencies of both the Au core and the Nb shell, namely, an intensive and continuous bathochromic spectral feature emerges in the red-NIR region (Fig. 2h). Evidently, this does not originate from the Au@Nb CS-NPs. One should therefore take another key component in Au@Nb@ $H_xK_{1-x}NbO_3$ NPPs into account, viz. is the niobate NSs. Bringing the metallic nanoantennas into contact with a dielectric NS, unlike the metal-metal interaction, generally leads to a redshift of the SPR^{22,23,53}. This is illustrated by the SPR absorption of the Au@Nb@ $H_xK_{1-x}NbO_3$ NPPs in comparison to the uncovered Au core (yellowish tinted region in Fig. 2h). The absorption band in the red-NIR region; however, cannot yet be reasonably explained.

Taken together, we could neither call the individual ingredients nor an overall combination in a NPP to account for its peculiar red-NIR absorption. In other words, only the biomimicry of the peapod design, and especially, its specific configurational traits, that differ significantly from known peapod structures, are responsible for this absorption band (Fig. 2i–k)^{44–46}. Thus, the diameter of the Au@Nb CS-NPs is highly monodisperse with an average of 9 nm (Fig. 2i), and the CS-NPs are intensively accumulated ranging from dimers to most often observed heptamers (Fig. 2j) that show uniform interparticle distances of about 2 nm (Fig. 2k). Even more important, this interparticle distance is small in relation to the Au@Nb CS-NPs size and well below the theoretically suggested threshold to induce a desirable electric near-field coupling⁴⁷. Such near-field coupling effect resembles the longitudinal SPR (LSPR) mode of an anisotropic Au nanoantenna and promotes an additional absorption band at wavelengths longer than the intrinsic transverse-mode SPR (TSPR) frequency (530 nm) of the Au NPs^{47–50}. The uniaxially aligned Au@Nb CS-NPs result in a field enhancement

particularly along the chain and lead to a LSPR-analogue absorption overwhelming nearly the entire red-NIR regime up to 800 nm.

Photocatalytic dye decomposition. So far, we have specified the configuration-dependent SPR effect of the Au@Nb@ $H_xK_{1-x}NbO_3$ NPPs endowed with a broadband light harvesting ability. Next, photocatalytic dye decomposition was carried out to substantiate the effect of comprehensive photon accumulation to enhance the useful charge carrier concentration for chemical reactions (Fig. 3). The experiments were carefully designed by using a UV cutoff filter and colored glass filters ($\lambda > 610$ nm) (Fig. 3a–c) to distinguish the plasmon-initiated carriers from those originating from the semiconductor. Moreover, methylene blue (MB) and Rhodamine B (RhB) were employed as the probing molecules to avoid the photosensitized dye perturbing the evaluation (see Methods section for details)^{34,55,56}.

In all cases, the presence of the Au@Nb CS-NPs substantially accelerates the $H_xK_{1-x}NbO_3$ NS semiconductor to bleach the dye solutions (Fig. 3d–f). The highest decoloring efficiency is observed in the case of the Au@Nb@ $H_xK_{1-x}NbO_3$ NPPs under full solar illumination (Fig. 3d). Evidently, the charge carriers involved in the chemical conversion only partly arise from the niobate NSs upon UV excitation. Moreover, the Au@Nb CS-NPs offer extra carriers upon SPR that is responsible for the acceleration (Fig. 3g–i). Taken together, the plasmonic nanoantennas boost the carrier quantity in either populating the energetic electrons originally residing on the metal to the adjacent semiconductor (direct electron transfer, DET) or in resonantly transferring its plasmonic energy to generate more e^-/h^+ pairs on the semiconductor (resonant energy transfer, RET)^{22,23,57,58}. Clearly, the enhancement in carrier concentration on the Au@Nb@ $H_xK_{1-x}NbO_3$ NPPs arises mostly from a DET in lieu of a RET process in terms of a minute spectral overlap between the Au NPs and the $H_xK_{1-x}NbO_3$ NSs (Fig. 2h). In a DET process, electrons of a plasmonic metal receive energy from an interacting photon followed by traversing a metal-semiconductor interface—the Schottky interface to migrate into the CB of the semiconductor. On this basis, the internal quantum transmission probability (η_i) for electron injection can be formulated by a modified Fowler equation^{59,60},

$$\eta_i \propto \frac{(h\nu - q\phi_b)^2}{h\nu}, \quad (2)$$

where $h\nu$ is the incident photon energy, and where $q\phi_b$ is the barrier height of the Schottky junction. The barrier height is established by electronic alignment between the Fermi level of the plasmonic metal and the flat-band potential (V_{fb}) of the coupled semiconductor. Herein, the work function of the Au@Nb CS-NPs is located in a spectrum with Au (~ 5.1 eV) and Nb (~ 4.3 eV) standing at the ends⁶¹. Given the insignificant fraction of a thin Nb shell in the Au@Nb CS-NPs (Fig. 2), the work function is primarily dictated by Au with a value close to 5.1 eV. V_{fb} of the $H_xK_{1-x}NbO_3$ semiconductor was estimated by the equation reported by Scaife et al.⁶² for oxides that do not contain metal cations with partially filled d -orbital as follows,

$$V_{fb}(\text{vs. NHE}) = 2.94 - E_g, \quad (3)$$

where E_g is the bandgap of the semiconductor. Consequently, a V_{fb} of -0.13 V (vs. NHE) for the $H_xK_{1-x}NbO_3$ NSs and a barrier height of ~ 0.7 eV for the Schottky junction between the Au@Nb CS-NPs and the $H_xK_{1-x}NbO_3$ NSs were derived. Surprisingly, this energy barrier is nearly one quadrant of the bandgap of the $H_xK_{1-x}NbO_3$ semiconductor, which is the key to allow photons that are invisible to the niobate, to produce active carriers to be used in chemical reactions. More significantly, the strong peapod-

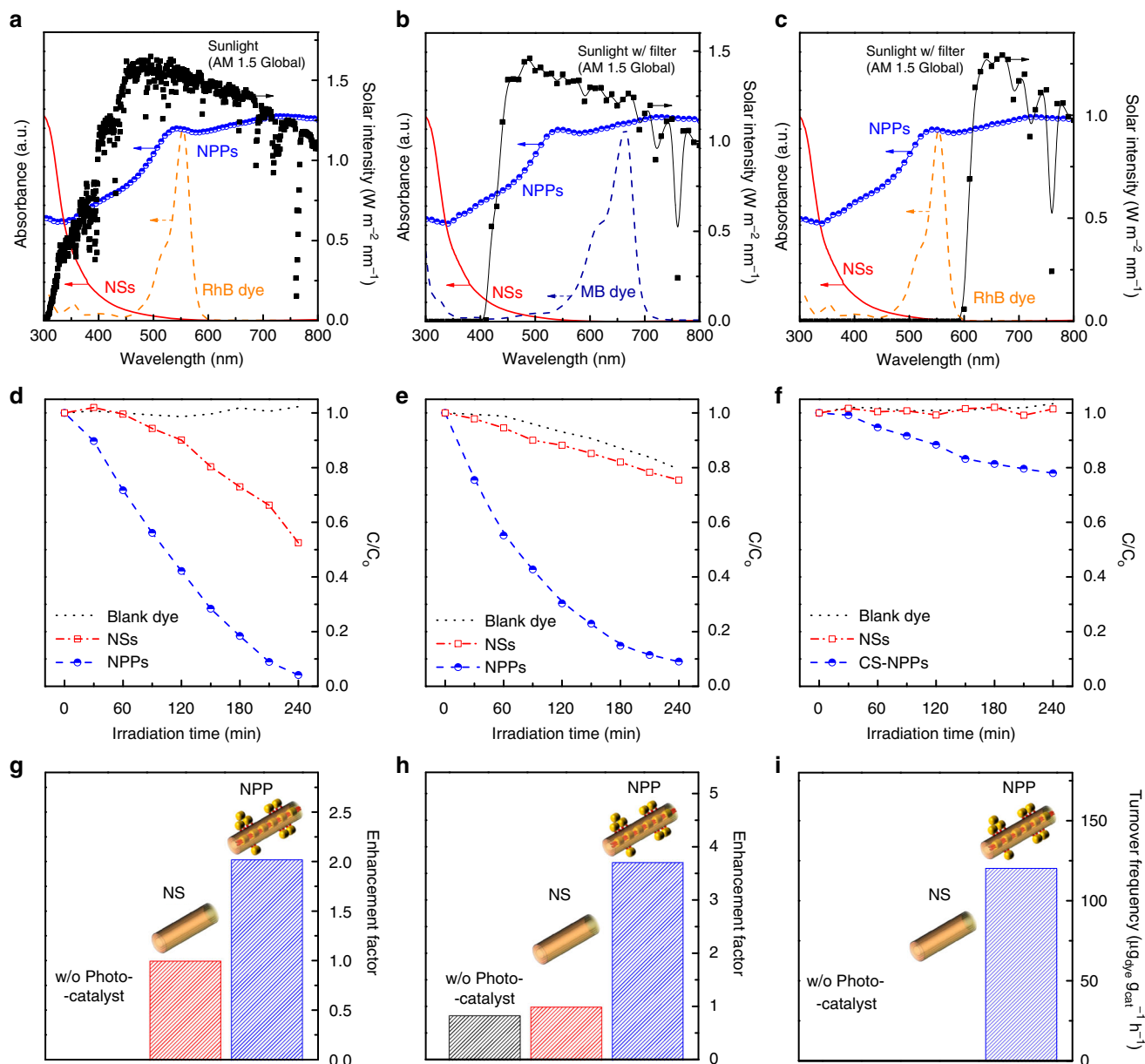


Fig. 3 Broadband photocatalytic activity of the Au@Nb@H_xK_{1-x}NbO₃ NPPs. **a–c** Spectra of simulated sunlight **(a)** further equipped with either an UV cutoff filter **(b)** or a colored glass filter **(c)** that work as irradiation sources for photocatalytic dye degradation. Absorption spectra of the employed H_xK_{1-x}NbO₃ NSs (solid line) and the Au@Nb@H_xK_{1-x}NbO₃ NPPs (half-filled circles) as photocatalysts; methylene blue (MB) and rhodamine B (RhB) as probing species (dashed line) are plotted alongside for reference. **d–f** Photocatalytic decoloring of RhB **(d, f)**, and MB **(e)** in the absence (dotted line) or in the presence of either niobate NSs (empty squares) or Au@Nb@H_xK_{1-x}NbO₃ NPPs (half-filled circles). **g–i** Comparison of the wavelength-dependent photoactivity between H_xK_{1-x}NbO₃ NSs and Au@Nb@H_xK_{1-x}NbO₃ NPPs under illumination with full solar light **(g)**, visible-NIR integral light **(h)**, and red-NIR integral light **(i)**, respectively. Abbreviations used: MB, methylene blue; RhB, Rhodamine B; NSs, nanoscrolls; NPPs, nanopapods; NIR, near-infrared

specific T- and L-SPR phenomena (Fig. 2h) permit visible- and NIR-photons to efficiently lend electrons on Au@Nb CS-NPs sufficient energy to enter the H_xK_{1-x}NbO₃ NSs and to contribute to the dye degradation⁶³. This prima facie evidence is given by the steady and efficient photobleaching courses (Fig. 3e, f).

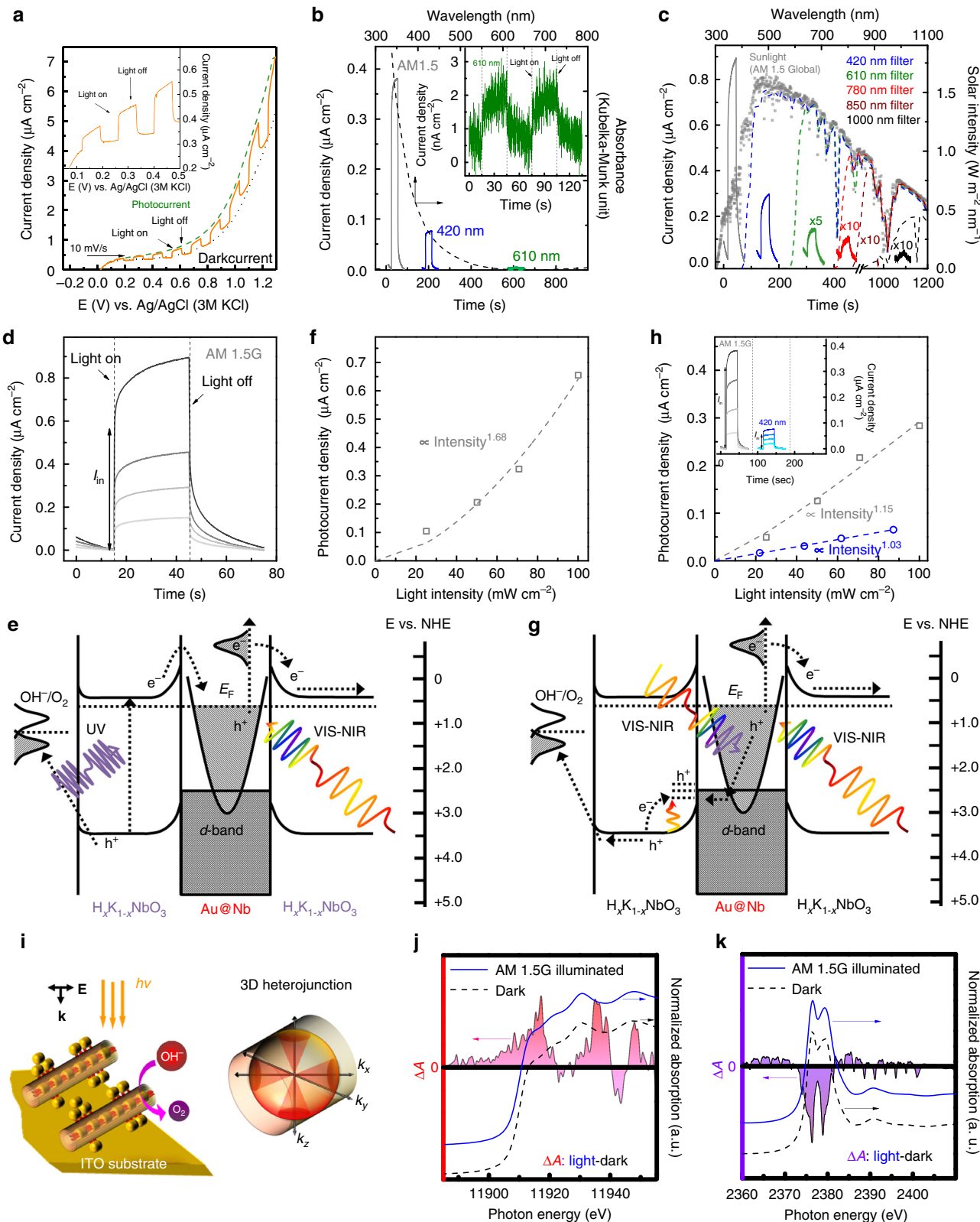
Photoelectrochemical water splitting. In addition to the fundamental dye degradation study, the Au@Nb@H_xK_{1-x}NbO₃ NPPs were examined in view of the photoelectrochemical (PEC) water splitting to corroborate the ability of the SPR-initiated photoinduced carriers in transferring solar energy into useful chemical fuels. In such artificial photosynthesis process (i.e., 2H₂O → 2H₂ + O₂), highly valuable H₂ molecules are produced

under sunlight³, which highlights the merit of employing this reaction for evaluation. The evaluation of the respective photon energy storage efficiency is deduced from the overall reaction rate, which was mostly expressed by the photoinduced current flowing from the Au@Nb@H_xK_{1-x}NbO₃ photoelectrode (Methods section). It is to be noted that an argon-purged aqueous solution containing 0.5 M Na₂SO₄ was used as the electrolyte and no sacrificial agent was present.

The specific photocurrent-potential response of the Au@Nb@H_xK_{1-x}NbO₃ photoelectrode was first characterized under chopped full solar illumination at a fluence of 100 mW cm⁻² (Fig. 4a). The anodic photocurrent was first perceived at about 0.1 V (Fig. 4a) and raises steadily to 0.9 μA cm⁻² at 1 V (i.e.,

potentials on the Ag/AgCl scale). The enhancement upon anodic polarization stems from the reinforced band bending within the space-charge layer of the outmost $H_xK_{1-x}NbO_3$ NSs which effectively rectifies the carrier transport (Supplementary Fig. 6a, b, see Supplementary Note 2 for details)⁶⁴. This anodically biased photocurrent doubles the performance of the $H_xK_{1-x}NbO_3$ photoelectrode under the same conditions (Fig. 4b, c). Even

more important, the photocurrent enhancement multiplies significantly upon modulating the irradiation wavelength. The enhancement factor calculated as the photocurrent of the $Au@H_xK_{1-x}NbO_3$ NPP photoelectrode divided by that of the $H_xK_{1-x}NbO_3$ NS photoelectrode is threefold below the integral of VIS-NIR light illumination and reaches one order of magnitude below the broadband red-NIR light illumination. Most



surprisingly, the maximum improvement is achieved under NIR light irradiation alone, even though its photon energy (<1.8 eV) is far below that of visible (2–3 eV) and UV (>3 eV) photons. Moreover, the characteristic photocurrent-time response of the Au@Nb@H_xK_{1-x}NbO₃ photoelectrode was monitored (at 1 V vs. Ag/AgCl), in which the photocurrent shows an intriguing transient behavior (Fig. 4d). In the light-on period, the photocurrent demonstrates an initial shoot (*I*_{in}) followed by a steady raise mimicking the rectangular signal that is expected in an ideal case⁶⁴. This variation implies a non-equilibrium between the carrier generation rate under light casting and its consumption rate upon reacting with water molecules. Several probable mechanisms may account for that and are inspected in detail below.

Considering the thermodynamically ($\Delta_r G^0 = +472 \text{ kJ mol}^{-1}$) and kinetically (four-electron oxidation: $2\text{H}_2\text{O} \rightarrow 2\text{O}_2 + 4\text{H}^+ + 4\text{e}^-$) unfavorable cleavage of water, the poor water oxidation on the Au@Nb@H_xK_{1-x}NbO₃ NPP photoelectrode can influence the PEC performance. For this reason, 1 M Na(COOH) was added to the electrolyte to modify the overall reaction mechanism. The oxidation of formate is comparably easy (one-electron oxidation: $[\text{HCOO}]^- \rightarrow \text{CO}_2 + \text{H}^+ + \text{e}^-$)⁶⁵. As a consequence, the photocurrent is nearly doubled in the presence of Na(COOH) (Supplementary Fig. 7a–c, see Supplementary Note 2 for details). Nonetheless, the independence of the photocurrent transient implies that the reaction kinetics of the chemical reaction is not the major contribution. In other words, the charge-carrier generation kinetics is responsible for the phenomenon. This finding encourages us to postulate the following mechanism for the different photocurrent response (Fig. 4d). Under broadband sunlight illumination, charge carriers occur simultaneously on the H_xK_{1-x}NbO₃ NS semiconductor and the Au@Nb CS-NP nanoantenna upon UV and integral VIS-NIR light excitation (Fig. 4e). The SPR-mediated energetic electrons on the Au@Nb CS-NPs become the charge carriers on the H_xK_{1-x}NbO₃ NS semiconductor via the DET process^{57,58}. An external bias then dictates these charges, including the metal-injected and the semiconductor-originating electrons—to move to the Pt electrode for water reduction to H₂³. Meanwhile, the photogenerated hole on the H_xK_{1-x}NbO₃ NS semiconductor is scavenged by the surrounding aqueous medium to generate O₂ on the Au@Nb@H_xK_{1-x}NbO₃ NPP photoanode (Supplementary Figs. 8 and 9, see Supplementary Note 2 for details). Finally, a second UV photon produces the next e⁻/h⁺ pair on the H_xK_{1-x}NbO₃ NS semiconductor followed by an electron transfer to a Au@Nb CS-

NP to compensate the accumulated hole and to complete the overall process^{66,67}.

The above process suggests a linear dependency of the photocurrent on the intensity of incident simulated sunlight (see Supplementary Note 3 for details), which, however, is in significant contrast to the superlinear behavior shown in Fig. 4f. The quasi-quadratic correlation indicates a nonlinear effect in the process of the photohole compensation. In brief, the electron vacancies on the Au@Nb CS-NPs are first subjected to an excitation process to a lower energy state in the *d*-band on the Au@Nb CS-NPs upon electron transition of the subsequently incident photon (Fig. 4g). This view is strongly supported by Jiang et al.⁶⁸ who reported on a similar phenomenon regarding the photoluminescence of anisotropically coupled Au NPs. The overall process—designated as two sequential one-photon absorption in the literature—starts with a first VIS-/NIR-photon inducing a *sp* → *sp* intraband transition to create an electron vacancy below the Fermi level of certain plasmonic nanostructure, which is in analogy to the SPR-mediated hot-electron generation process on the Au@Nb CS-NPs in our study. The second photon then excites an electron from the *d*- to the *sp*-band via an interband transition to transfer the hole to the *d*-band. According to Jiang et al.⁶⁸, the *d*-band hole recombines with the electron in the *sp*-band, giving rise to photoluminescence. In contrast, the photocurrent response in our study indicates that the hole is retrieved by the coupled H_xK_{1-x}NbO₃ NS semiconductor, and thereafter it participates in water oxidation in preference to charge recombination.

In this hole recovery, energy states associated to H_xK_{1-x}NbO₃ defects at the interface between the Au@Nb CS-NPs and the H_xK_{1-x}NbO₃ NSs play an important role. The surface states originate mostly from the stepwise nano-texturization of the H_xK_{1-x}NbO₃ NSs, as evidenced by the absorption spectra (i.e., the inefficient absorbance at wavelengths beyond the band gap) and the photocurrent-time plot (i.e., the photocurrent response under sub-bandgap integral VIS-NIR light irradiation). In general, these mid-gap electronic states are identified with a shallow energy position close to the valence band (VB) edge, which favors them to serve as a hole relay to facilitate the extraction^{58,64}. Afterwards, a thermal transition brings the hole from this trapped state to the VB of the H_xK_{1-x}NbO₃ NS semiconductor, where it drifts to the surface and reacts with water molecules to generate O₂. This cascade-type charge delivery explains the superlinearity of the transient photocurrent response of the Au@Nb@H_xK_{1-x}NbO₃ NPP photoelectrode on the light intensity. Noteworthy, the probability of the intraband transition predominates that of the

Fig. 4 Photoelectrochemical water splitting with the Au@Nb@H_xK_{1-x}NbO₃ NPP photoelectrode. **a** Current-potential characteristics of the Au@Nb@H_xK_{1-x}NbO₃ photoelectrode in 0.5 M Na₂SO₄ solution (pH 6.8) under chopped (orange line) and continuous (green dashed line) AM 1.5G simulated sunlight illumination. The dark current is plotted alongside (dark dotted line). **b, c** Wavelength-dependent photocurrent-time plots (baseline subtracted) of a H_xK_{1-x}NbO₃ NS (**b**) and a Au@Nb@H_xK_{1-x}NbO₃ NPP photoelectrode (**c**) under irradiation of AM 1.5G simulated sunlight (gray line) equipped with different long-pass filters (colored solid lines) in the presence of an anodic bias of 1 V (vs. Ag/AgCl). Absorption spectra of the H_xK_{1-x}NbO₃ NSs (black dashed line in **b**) and AM 1.5G simulated sunlight (filled squares in **c**) illumination after passing a UV cutoff filter (blue dashed line in **c**) or different colored glass filters (green, red, brown, and black dashed line in **c**) are plotted alongside for comparison. **b** Photocurrent-time plot (baseline subtracted) of the H_xK_{1-x}NbO₃ NS photoelectrode under integral red-NIR illumination in the presence of an anodic bias of 1 V (vs. Ag/AgCl). **d** Fluence-dependent photocurrent-time plots (baseline subtracted) of the Au@Nb@H_xK_{1-x}NbO₃ NPP photoelectrode. **e** Postulated charge transfer on the Au@Nb@H_xK_{1-x}NbO₃ NPP heterojunction starts with the photoabsorption process. **f** *I*_{in} as a function of simulated sunlight intensity of the Au@Nb@H_xK_{1-x}NbO₃ NPP photoelectrode. **g** Postulated charge transfer on the Au@Nb@H_xK_{1-x}NbO₃ NPP heterojunction via a two sequential one-photon absorption process. **h** *I*_{in} as a function of the intensity of either simulated sunlight (gray line) or integral VIS-NIR light (blue line) for the H_xK_{1-x}NbO₃ NS photoelectrode. **i** Fluence-dependent photocurrent-time plots (baseline subtracted) of the H_xK_{1-x}NbO₃ NS photoelectrode. **j** Schematic illustration of the 3D metal-semiconductor heterojunction of the Au@Nb@H_xK_{1-x}NbO₃ NPP photoelectrode. **j, k** Normalized Au (**j**) and Nb (**k**) L₃-edge XAS spectra of the Au@Nb@H_xK_{1-x}NbO₃ NPPs collected in the presence and absence of AM 1.5G simulated sunlight. The difference in absorbance (ΔA) between the aforementioned two conditions is plotted alongside. Abbreviations used: NS, nanoscroll; NPP, nanopapod; VIS, visible, NIR, near-infrared, *I*_{in}, initial photocurrent shoot at the light-on instant; *E*_F, Fermi level; **E**, electric field, **k**, wavenumber; ITO, tin-doped indium oxide

interband transition in the very beginning of the light-on phase, because the electron density in the *sp* band is much higher than that of the photogenerated *sp* band vacancy. Afterwards, the quantitative surge in the *sp*-band hole in turn reinforces the probability of the interband transition (Supplementary Fig. 10a–f, see Supplementary Note 3 for details), which is responsible for the current rise following I_{in} in the photocurrent-time plot (Fig. 4d).

Despite of the photohole transfer subjected to the above described cascade mechanism, the photocurrent response is yet clearly visible under NIR light illumination (Fig. 4c). This implies a significantly mitigated recombination of antipodal charge carriers. In particular, such carrier loss in the volume of the $H_xK_{1-x}NbO_3$ NSs is efficiently suppressed, as evidenced by the quasi-linear dependency demonstrated by the $H_xK_{1-x}NbO_3$ photoelectrode without plasmonic Au@Nb nanoantennas (Fig. 4h). This can be attributed to the depletion region developed due to the applied bias that nearly overwhelms the complete niobate NS (Supplementary Fig. 6a, b, see Supplementary Note 2 for details). Likewise, the carrier decay in the SPR excitation process is significantly quenched, which most likely relates to rapid spatial separation at the instant of the hot-electron generation. One should keep in mind that the isolation of the hot electron with an energy exceeding the Schottky-barrier height has to reach the metal-semiconductor interface to allow the DET process⁵⁹. This propagation of a hot electron requests a momentum change (Δk) that is harvested from the wavevector (*k*-vector) of the incident photon with additional support of a phonon or an imperfection⁶⁹. Such defect-assisted propagation suggests that the energetic electrons are preferentially formed at the margin of the sub-10-nm-sized Au@Nb CS-NPs due to the enormous imperfection area available at the boundary of the $H_xK_{1-x}NbO_3$ NSs and the plasmonic CS-NPs. Herein, a considerable bridge area offered by the peapod-specific 3D metal-semiconductor interface greatly favors the $H_xK_{1-x}NbO_3$ semiconductor to immediately collect those spatially localized hot electrons (Fig. 4i)^{30,35}. Moreover, an energy dissipation due to electron collision is also circumvented and results in a high-DET efficiency. To this concern, X-ray absorption spectroscopy (XAS) at the Au and Nb L_3 -edge—describing the empty Au $5d/6s-p$ hybridized orbitals and the unoccupied Nb $4d$ states being most responsible for the CB nature of the $H_xK_{1-x}NbO_3$ —was employed to study the performance. At first sight, a clearly increased absorbance is evidenced by Au L_3 -edge XAS after simultaneously irradiation with simulated sunlight, which indicates an additional electron transition from the Au $2p$ to the *s-p-d* hybridization orbitals by soft X-rays (Fig. 4j). This finding implies that additional electron vacancies are formed in this hybridized band. Concurrently, Nb L_3 -edge XAS shows a decreased absorbance that suggests reduced empty states in the Nb $4d$ orbital being available to X-ray excited electrons from the Nb $2p$ state (Fig. 4k). Otherwise, the CB of $H_xK_{1-x}NbO_3$ is occupied. Such inverted absorbance of the Au and the Nb L_3 -edge XAS reveals substantial evidence for the conversion of SPR-mediated hot electrons into the CB of $H_xK_{1-x}NbO_3$ and validates their spatial isolation from the geminate photoholes⁷⁰. Overall, the synergism between the rapid DET process and the cascade hole delivery is illustrated by the constant photocurrent flow at the incidence of modulated sunlight.

In summary, an alternative promising configuration of a plasmonic photocatalyst design is introduced emulating the growth pattern of a natural plant—a peapod. Spherical Au@Nb core-shell plasmonic nanoantennas with a nanometric break in between are unidirectionally deposited inside the cavity of a tubular $H_xK_{1-x}NbO_3$ semiconductor. In particular, the biomimicry of this peapod design induces a strong interantenna electric near-field coupling that endows the Au@Nb@ $H_xK_{1-x}NbO_3$ nanopeapod photocatalyst with a NIR photon harvesting ability.

More importantly, the collected NIR photons are exclusively transferred into energetic charge carriers via a direct electron transfer (DET) process to promote highly relevant chemical reactions, such as the degradation of organic dyes or water splitting (see Supplementary Note 4 for details).

For both organic dye degradation and water splitting, the photoactivity of the Au@Nb@ $H_xK_{1-x}NbO_3$ nanopeapod photocatalyst outperforms a photocatalyst without Au@Nb nanoantenna significantly. The enhancement stems mostly from the synergistic effect between (i) a rapid DET process due to the appreciable interfacial area provided by a peapod-specific 3D metal-semiconductor junction boosting hot-electron collection, and (ii) a cascade hole delivery supported by a sequential two-photon-assisted hole excitation process with rapid hole injection into the $H_xK_{1-x}NbO_3$ semiconductor that is mediated by a mid-gap relay state. Taken together, the results suggest that the biomimetic pattern holds a great promise as a key design for widespread photoactive devices involving the use of NIR photons. This includes phototheranostic agents, optical sensors, plasmonic waveguides, broadband solar cells and so forth.

Methods

Fabrication of the $H_xK_{1-x}NbO_3$ nanocrystals. Templated $K_4Nb_6O_{17}$ was prepared by a solid-state reaction, in which reagent-grade K_2CO_3 and Nb_2O_5 (99.99%) with a molar ratio of 1.1:1.5 were first ground together and heated in an alumina crucible at 900 °C for 1 h before continuing to 1050 °C for another 24 h. A slight excess of K_2CO_3 (10 mol-%) was employed to compensate for any material volatilized during heating. The cooling product was washed three times with distilled water and acetone respectively and dried in the oven overnight. The as-prepared $K_4Nb_6O_{17}$ was next immersed in a warm (60 °C) and concentrated (3 mol/L) HCl solution for at least 4 days to obtain the proton-exchanged hexaniobates ($H_xK_{1-x}Nb_6O_{17}$). After the acid-treatment, the product was centrifuged and washed with distilled water and acetone, three times in each case, and dried overnight. Templated phase transformation from $H_xK_{4-x}Nb_6O_{17}$ to $H_xK_{1-x}NbO_3$ and concurrent NS formation were carried out based on a solvothermal process reported by Adireddy et al.⁴⁰ with some modifications. Experimental conditions were described below, the reaction solution was prepared by putting $H_xK_{4-x}Nb_6O_{17}$ (0.5 g), tetrabutylammonium hydroxide hydrate (TBAOH·30H₂O, 0.75 g, 0.95 mmol) and oleylamine (OAm, 25 mL, ~75 mmol) together in 40 mL toluene. This mixture was magnetically stirred at ambient temperature for 1 h before transferring into a Teflon-lined stainless steel autoclave. The autoclave was then maintained at 220 °C (ramping rate = 2 °C/min) for 6 h and followed by naturally cooling. The resulting $H_xK_{1-x}NbO_3$ NSs were collected by centrifugation, washed with ethanol several times and then dried overnight.

Synthesis of the Au@Nb@ $H_xK_{1-x}NbO_3$ nanopeapods. In a standard synthesis, the preformed $H_xK_{1-x}NbO_3$ NSs (20 mg), HAuCl₄·4H₂O (10 mg, ~0.025 mmol), oleic acid (OAc, 160 μL, 0.5 mmol), and OAm (165 μL, 0.5 mmol) were added to 3 mL hexane. The solution was then vigorously stirred and heated to nearly 60 °C for 24 h before cooling to room temperature. The color of the reacting mixture gradually turned from white to purple, suggesting the formation of Au@Nb CS-NPs inside $H_xK_{1-x}NbO_3$ NSs. The obtained composites were purified by a repetitive dispersion/precipitation cycle with ethanol and finally dispersed in either deionized water or hexane for subsequent photo(electro)catalytic examinations.

Analytical techniques. Samples for transmission electron microscopy (TEM) were prepared by casting one drop of hexane solution with Au@Nb@ $H_xK_{1-x}NbO_3$ NPPs onto a 300 mesh copper grid with carbon support film. The size, the morphology and the spatial distribution of Au@Nb CS-NPs and $H_xK_{1-x}NbO_3$ NSs in Au@Nb@ $H_xK_{1-x}NbO_3$ NPPs were investigated by high-resolution (HR) TEM performed with an aberration-corrected FEI Titan³ 80–300 microscope operated at 300 kV. Moreover, a Philips CM200 FEG/ST microscope operated at 200 kV was utilized to perform selected area electron diffraction (SAED) for crystal structure and phase identification. SAED patterns of NPPs often show only few and rather diffuse reflections on Debye-Scherrer rings at large reciprocal lattice distances. A way to prevent the loss of valuable diffraction information is achieved by azimuthally averaging the intensity of the SAED pattern (for short radial scans), which is obtained by a 2π intensity integration of each spatial frequency $k = |\mathbf{k}|$ in the initial SAED pattern. Radial scans can be used to investigate the structure on NPs similar to XRD patterns. Lattice parameters and crystal structure of NPP material are determined from radial scans by using the peak positions obtained by fitting a Voigt function to each individual peak profile after subtraction a linearly interpolated background. Alternatively, HRTEM images were evaluated by calculating the two-dimensional Fourier transform, denoted as diffractogram, which yields information on the crystal structure (lattice parameters and crystal

symmetry) of single nanoparticles. Crystal structure analyses was performed by comparing the experimental diffractograms and calculated diffraction patterns with Miller indices, where the latter were obtained by using the JEMS software. The absorption spectra of $H_xK_{1-x}NbO_3$ NSs and $Au@Nb@H_xK_{1-x}NbO_3$ NPPs were measured using a Varian Cary 100 Spectrometer and further analyzed by means of Kubelka-Munk transformation. For comparison, the ligand-stabilized Au NPs were additionally prepared in the same procedure as the fabrication of $Au@Nb@H_xK_{1-x}NbO_3$ NPPs but devoid of $H_xK_{1-x}NbO_3$ NSs. The as-obtained Au NPs were stored in hexane to collect an extinction spectrum.

Photocatalytic dye decomposition measurements. The photocatalytic activities of $Au@Nb@H_xK_{1-x}NbO_3$ NPPs and $H_xK_{1-x}NbO_3$ NSs were evaluated based on the enhancement in degradation rate of Rhodamine B (RhB) and methylene blue (MB) at their presence. The reaction was carried out in a Pyrex reaction cell containing a suspension of the photocatalyst powder (50 mg) in 100 mL aqueous dye solution with continuous agitation using a magnetic stirrer. The employed dye concentration was 5.44 mg/L while a threefold diluted solution was used in evaluating the photoactivity under red-NIR light illumination. Before illumination, the suspensions were magnetically stirred in the dark for 1 h to ensure the establishment of an adsorption/desorption equilibrium of dyes on the photocatalyst surface. Afterwards, the reactions were conducted under irradiation of simulated AM 1.5 G solar light (100 mW/cm) using a LOT Class ABA solar simulator (type LS0805) as the light source. For the measurements under visible-NIR or red-NIR light, an additional UV cutoff ($\lambda > 420$ nm) or colored glass filter ($\lambda > 610$ nm) was used, respectively. The UV cutoff filter was employed to distinguish carriers produced by the UV-active $H_xK_{1-x}NbO_3$ semiconductor from the plasmon-initiated carriers. Moreover, the colored glass filter was deployed to subdivide the SPR-initiated carrier formation into the visible-responsive transverse mode and the red-NIR-sensitive longitudinal mode, respectively. Since a charge transfer via the photosensitized dye may perturb reliable evaluation of the aspired SPR-boosted photon-to-carrier conversion efficiency in a dye degradation study, special attention needed to be paid to the probing molecules⁵⁵. Herein, MB was chosen owing to the energetic mismatch between the lowest unoccupied molecular orbital (LUMO) of MB and the CB edge of the $H_xK_{1-x}NbO_3$ semiconductor^{34,56}. Moreover, RhB was selected to investigate the activity of LSPR-promoted carriers and to avoid competitive photon absorption by the dye as evidenced in the absorption spectra showing that a colored glass filter can efficiently exclude eventual self-absorption of RhB (Fig. 3c). The experiments were carried out at room temperature in air. At each 30 min, 2 mL of aliquot was collected from the reactor. The catalysts were separated by centrifugation and the dye solutions were analyzed by UV-Vis spectrophotometry. The concentration evolution of the dye solution was monitored based on the intensity variation in the featured absorption peak of dyes (λ_{abs} of RhB and MB are 554 and 664 nm, respectively).

Photoelectrochemical water splitting characterizations. The measurement was carried out in an undivided either two- or a three-electrode cell configuration, employing either $Au@Nb@H_xK_{1-x}NbO_3$ NPPs or $H_xK_{1-x}NbO_3$ NSs as the working electrode subjected to the irradiation, a Pt coil or Pt foil as the counter electrode and an additional silver/silver chloride reference electrode (Ag/AgCl in 3 M KCl, 0.207 V vs. NHE) was applied for the three-electrode setup. The photoelectrodes were fabricated upon drop-casting 100 μ L $Au@Nb@H_xK_{1-x}NbO_3$ NPP/ $H_xK_{1-x}NbO_3$ NS suspension (20 mg NPP/NS in 1 mL hexane) onto an indium tin oxide (ITO) conducting substrate without post-thermal and -chemical treatments. A potentiostat (CH Instruments, CHI 627D) was used for monitoring the photo-current behaviors as a function of either potential or time, respectively. A simulated AM 1.5G solar light was used as the irradiation source and the light intensity was calibrated to 100 mW/cm (1 sun). The photocurrent-potential plots were obtained with a potential window from -0.25 to +1.3 V (on the Ag/AgCl scale) at a potential sweeping rate of 10 mV/s. The photocurrent-time plots were recorded at 1 V (vs. Ag/AgCl) with different irradiation wavelengths. For the wavelength-dependent measurement, a UV cutoff filter ($\lambda > 420$ nm) was employed to eliminate UV light, and different colored glasses ($\lambda > 610$ nm) were used to progressively filter the integral UV to visible light. The incident light was casting on the photoelectrode from the back side through a quartz window and the electrolyte. Argon-purged aqueous solutions containing either 0.5 M Na_2SO_4 or 0.5 M Na_2SO_4 and 1 M Na (COOH) were used as the electrolytes.

Data availability. The data that support the findings of this study are available from the corresponding author upon reasonable request.

Received: 21 April 2017 Accepted: 19 December 2017

Published online: 16 January 2018

References

- Barber, J. Photosynthetic energy conversion: natural and artificial. *Chem. Soc. Rev.* **38**, 185–196 (2009).
- Long, S. P., Marshall-Colon, A. & Zhu, X. G. Meeting the global food demand of the future by engineering crop photosynthesis and yield potential. *Cell* **161**, 56–66 (2015).
- Tachibana, Y., Vayssieres, Y. & Durrant, J. R. Artificial photosynthesis for solar water-splitting. *Nat. Photon.* **6**, 511–518 (2012).
- Roy, S. C., Varghese, O. K., Paulose, M. & Grimes, C. A. Toward solar fuels: photocatalytic conversion of carbon dioxide to hydrocarbons. *ACS Nano* **4**, 1259–1278 (2010).
- Faunce, T. A. et al. Energy and environment policy case for a global project on artificial photosynthesis. *Energy Environ. Sci.* **6**, 695–698 (2013).
- Chen, Y. C. et al. β -SnWO₄ photocatalyst showing controlled morphological transition of cubes to spikecubes. *ACS Catal.* **6**, 2357–2367 (2016).
- Linic, S., Aslam, U., Boerigter, C. & Morabito, M. Photochemical transformations on plasmonic metal nanoparticles. *Nat. Mater.* **14**, 567–576 (2015).
- Lin, Y. G. et al. Hierarchically porous Ca-containing MnO₂ nanorod bundles with superior photoelectrochemical activity. *ChemCatChem* **6**, 1684–1690 (2014).
- Wang, Q. et al. Scalable water splitting on particulate photocatalyst sheets with a solar-to-hydrogen energy conversion efficiency exceeding 1%. *Nat. Mater.* **15**, 611–615 (2016).
- Lin, Y. G. et al. Cobalt-phosphate-assisted photoelectrochemical water oxidation by arrays of molybdenum-doped zinc oxide nanorods. *ChemSusChem* **7**, 2748–2754 (2014).
- Tu, W. G., Zhou, Y. & Zou, Z. G. Photocatalytic conversion of CO₂ into renewable hydrocarbon fuels: state-of-the-art accomplishment, challenges, and prospects. *Adv. Mater.* **26**, 4607–4626 (2014).
- Hsu, Y. K., Fu, S. Y., Chen, M. H., Chen, Y. C. & Lin, Y. G. Facile synthesis of Pt nanoparticles/ZnO nanorod arrays for photoelectrochemical water splitting. *Electrochim. Acta* **120**, 1–5 (2014).
- Ghosh, S. et al. Conducting polymer nanostructures for photocatalysis under visible light. *Nat. Mater.* **14**, 505–511 (2015).
- Schultz, D. M. & Yoon, T. P. Solar synthesis: prospects in visible light photocatalysis. *Science* **343**, 1239176 (2014).
- Oshikiri, T., Ueno, K. & Misawa, H. Plasmon-induced ammonia synthesis through nitrogen photofixation with visible light irradiation. *Angew. Chem. Int. Ed.* **53**, 9802–9805 (2014).
- Moniz, S. J. A., Shevlin, S. A., Martin, D. J., Guo, Z. X. & Tang, J. W. Visible-light driven heterojunction photocatalysts for water splitting—a critical review. *Energy Environ. Sci.* **8**, 731–759 (2015).
- Hsu, Y. K., Chen, Y. C. & Lin, Y. G. Novel ZnO/Fe₂O₃ core-shell nanowires for photoelectrochemical water splitting. *ACS Appl. Mater. Inter.* **7**, 14157–14162 (2015).
- Sang, Y. et al. From UV to near-infrared, WS₂ nanosheet: a novel photocatalyst for full solar light spectrum photodegradation. *Adv. Mater.* **27**, 363–369 (2015).
- Zhang, X. et al. Visible/near-infrared-light-induced H₂ production over g-C₃N₄ cosensitized by organic dye and zinc phthalocyanine derivative. *ACS Catal.* **5**, 504–510 (2015).
- Nishijima, Y. et al. Near-infrared plasmon-assisted water oxidation. *J. Phys. Chem. Lett.* **3**, 1248–1252 (2012).
- Zheng, Z., Tachikawa, T. & Majima, T. Single-particle study of Pt-modified Au nanorods for plasmon-enhanced hydrogen generation in visible to near-infrared region. *J. Am. Chem. Soc.* **136**, 6870–6873 (2014).
- Zhang, X., Chen, Y. L., Liu, R. S. & Tsai, D. P. Plasmonic photocatalysis. *Rep. Prog. Phys.* **76**, 046401 (2013).
- Zhang, P., Wang, T. & Gong, J. L. Mechanistic understanding of the plasmonic enhancement for solar water splitting. *Adv. Mater.* **27**, 5328–5342 (2015).
- Knight, M. W., Sobhani, H., Nordlander, P. & Halas, N. J. Photodetection with active optical antennas. *Science* **332**, 702–704 (2011).
- Pescaglini, A. et al. Hot-electron injection in Au nanorod–ZnO nanowire hybrid device for near-infrared photodetection. *Nano Lett.* **14**, 6202–6209 (2014).
- Seo, E., Ko, S.-J., Min, S. H., Kim, J. Y. & Kim, B.-S. Plasmonic transition via interparticle coupling of Au@Ag core-shell nanostructures sheathed in double hydrophilic block copolymer for high-performance polymer solar cell. *Chem. Mater.* **27**, 4789–4798 (2015).
- Fang, Z. et al. Graphene-antenna sandwich photodetector. *Nano Lett.* **12**, 3808–3813 (2012).
- Mubeen, S. et al. An autonomous photosynthetic device in which all charge carriers derive from surface plasmons. *Nat. Nanotechnol.* **8**, 247–251 (2013).
- Kazuma, E., Sakai, N. & Tatsuma, T. Nanoimaging of localized plasmon-induced charge separation. *Chem. Commun.* **47**, 5777–5779 (2011).
- Knight, M. W. et al. Embedding plasmonic nanostructure diodes enhances hot electron emission. *Nano Lett.* **13**, 1687–1692 (2013).

31. Roy, P., Berger, S. & Schmuki, P. TiO₂ nanotubes: synthesis and applications. *Angew. Chem. Int. Ed.* **50**, 2904–2939 (2011).
32. Lin, Y. G., Hsu, Y. K., Lin, Y. C. & Chen, Y. C. Hierarchical Fe₂O₃ nanotube/nickel foam electrodes for electrochemical energy storage. *Electrochim. Acta* **216**, 287–294 (2016).
33. Maeda, K., Eguchi, M., Youngblood, W. J. & Mallouk, T. E. Niobium oxide nanoscrolls as building blocks for dye-sensitized hydrogen production from water under visible light irradiation. *Chem. Mater.* **20**, 6770–6778 (2008).
34. Kudo, A. & Miseki, Y. Heterogeneous photocatalyst materials for water splitting. *Chem. Soc. Rev.* **38**, 253–278 (2009).
35. Clavero, C. Plasmon-induced hot-electron generation at nanoparticle/metal-oxide interfaces for photovoltaic and photocatalytic devices. *Nat. Photon.* **8**, 95–103 (2014).
36. Pribosic, I., Makovec, D. & Drogenik, M. Formation of nanoneedles and nanoplatelets of KNbO₃ perovskite during templated crystallization of the precursor gel. *Chem. Mater.* **17**, 2953–2958 (2005).
37. Kong, X. G. et al. Transformation of potassium Lindquist hexaniobate to various potassium niobates: solvothermal synthesis and structural evolution mechanism. *Dalton Trans.* **42**, 7699–7709 (2013).
38. Saupé, G. B. et al. Nanoscale tubules formed by exfoliation of potassium hexaniobate. *Chem. Mater.* **12**, 1556–1562 (2000).
39. Kobayashi, Y., Hata, H., Salama, M. & Mallouk, T. E. Scrolled sheet precursor route to niobium and tantalum oxide nanotubes. *Nano Lett.* **7**, 2142–2145 (2007).
40. Adireddy, S., Yao, Y., He, F. & Wiley, J. B. Rapid solvothermal fabrication of hexaniobate nanoscrolls. *Mater. Res. Bull.* **48**, 3236–3241 (2013).
41. Zhang, T. T. et al. Insights into the structure–photoreactivity relationships in well-defined perovskite ferroelectric KNbO₃ nanowires. *Chem. Sci.* **6**, 4118–4123 (2015).
42. Zhang, T. T. et al. Organic pollutant photodecomposition by Ag/KNbO₃ nanocomposites: a combined experimental and theoretical study. *J. Phys. Chem. C* **120**, 2777–2786 (2016).
43. Sarahan, M. C. et al. K₄Nb₆O₁₇-derived photocatalysts for hydrogen evolution from water: nanoscrolls versus nanosheets. *J. Solid State Chem.* **181**, 1678–1683 (2008).
44. Hu, M. S. et al. Photosensitive gold-nanoparticle-embedded dielectric nanowires. *Nat. Mater.* **5**, 102–106 (2006).
45. Hsieh, C. H., Chou, L. J., Lin, G. R., Bando, Y. & Golberg, D. Nanophotonic switch: gold-in-Ga₂O₃ peapod nanowires. *Nano Lett.* **8**, 3081–3085 (2008).
46. Qin, Y., Liu, L., Yang, R., Gosele, U. & Knez, M. General assembly method for linear metal nanoparticle chains embedded in nanotubes. *Nano Lett.* **8**, 3221–3225 (2008).
47. Harris, N., Arnold, M. D., Blaber, M. G. & Ford, M. J. Plasmonic resonances of closely coupled gold nanosphere chains. *J. Phys. Chem. C* **113**, 2784–2791 (2009).
48. Atay, T., Song, J. H. & Nurmikko, A. V. Strongly interacting plasmon nanoparticle pairs: from dipole-dipole interaction to conductively coupled regime. *Nano Lett.* **4**, 1627–1631 (2004).
49. Zhong, Z., Pakovskyy, S., Bouvrette, P., Luong, J. H. T. & Gedanken, A. The surface chemistry of Au colloids and their interactions with functional amino acids. *J. Phys. Chem. B* **108**, 446–4052 (2004).
50. Thomas, K. G., Barazzouk, S., Ipe, B. I., Joseph, S. T. S. & Kamat, P. V. Uniaxial plasmon coupling through longitudinal self-assembly of gold nanorods. *J. Phys. Chem. B* **108**, 13066–13068 (2004).
51. Adireddy, S. et al. Peapod-type nanocomposites through the in situ growth of gold nanoparticles within preformed hexaniobate nanoscrolls. *Angew. Chem. Int. Ed.* **53**, 4614–4617 (2014).
52. Kolb, D. M., Przasnyski, M. & Gerischer, H. Underpotential deposition of metals and work function differences. *Electro. Chem. Inter. Electrochem.* **54**, 25–38 (1974).
53. Cortie, M. B. & McDonagh, A. M. Synthesis and optical properties of hybrid and alloy plasmonic nanoparticles. *Chem. Rev.* **111**, 3713–3735 (2011).
54. Creighton, J. A. & Eadont, D. G. Ultraviolet-visible absorption spectra of the colloidal metallic elements. *J. Chem. Soc. Faraday Trans.* **87**, 3881–3891 (1991).
55. Yi, Z. G. et al. An orthophosphate semiconductor with photooxidation properties under visible-light irradiation. *Nat. Mater.* **9**, 559–564 (2010).
56. Shen, J. S., Yu, T., Xie, J. W. & Jiang, Y. B. Photoluminescence of CdTe nanocrystals modulated by methylene blue and DNA. A label-free luminescent signaling nanohybrid platform. *Phys. Chem. Chem. Phys.* **11**, 5062–5069 (2009).
57. Cushing, S. K. et al. Photocatalytic activity enhanced by plasmonic resonant energy transfer from metal to semiconductor. *J. Am. Chem. Soc.* **134**, 15033–15041 (2012).
58. Li, J. T. et al. Solar hydrogen generation by a CdS-Au-TiO₂ sandwich nanorod array enhanced with Au nanoparticle as electron relay and plasmonic photosensitizer. *J. Am. Chem. Soc.* **136**, 8438–8449 (2014).
59. Fowler, R. H. The analysis of photoelectric sensitivity curves for clean metals at various temperatures. *Phys. Rev.* **38**, 45–56 (1931).
60. Sze, S. M. & Ng, K. K. *Physics of Semiconductor Devices* (Wiley, Hoboken, NJ, USA, 2007).
61. Hölzl, J., Schulte, F. K. & Wagner, H. *Solid Surface Physics* (Springer, Berlin, Germany, 1979).
62. Scaife, D. E. Oxide semiconductors in photoelectrochemical conversion of solar energy. *Sol. Energy* **25**, 41–54 (1980).
63. Li, B. X. et al. (Gold core)@(ceria shell) nanostructures for plasmon-enhanced catalytic reactions under visible light. *ACS Nano* **8**, 8152–8162 (2014).
64. Salvador, P. Kinetic approach to the photocurrent transients in water photoelectrolysis at n-titanium dioxide electrodes. I. Analysis of the ratio of the instantaneous to steady-state photocurrent. *J. Phys. Chem.* **89**, 3863–3869 (1985).
65. Hsu, Y. K., Chen, Y. C., Lin, Y. G., Chen, L. C. & Chen, K. H. Birnessite-type manganese oxides nanosheets with hole acceptor assisted photoelectrochemical activity in response to visible light. *J. Mater. Chem.* **22**, 2733–2739 (2012).
66. Hirakawa, T. & Kamat, P. V. Charge separation and catalytic activity of Ag@TiO₂ core-shell composite clusters under UV-Irradiation. *J. Am. Chem. Soc.* **127**, 3928–3934 (2005).
67. Jakob, M., Levanon, H. & Kamat, P. V. Charge distribution between UV-irradiated TiO₂ and gold nanoparticles: determination of shift in the fermi level. *Nano Lett.* **3**, 353–358 (2003).
68. Jiang, X. F. et al. Excitation nature of two-photon photoluminescence of gold nanorods and coupled gold nanoparticles studied by two-pulse emission modulation spectroscopy. *J. Phys. Chem. Lett.* **4**, 1634–1638 (2013).
69. Shalae, V. M., Douketis, C., Stuckless, J. T. & Moskovits, M. Light-induced kinetic effects in solids. *Phys. Rev. B* **53**, 11388–11402 (1996).
70. Hung, S. F. et al. Iridium oxide-assisted plasmon-induced hot carriers: improvement on kinetics and thermodynamics of hot carriers. *Adv. Energy Mater.* **6**, 1501339 (2016).

Acknowledgements

The authors gratefully thank the German Research Society (DFG), Germany, for funding of equipment. We also acknowledge the Ministry of Science and Technology (MOST) and the National Synchrotron Radiation Research Center (NSRRC), Taiwan, for financial support under contracts MOST 103–2112-M-213–001-MY2, 105–2221-E-259–024-MY3, and 105–2221-E-259–026. Y.-C.C. acknowledges support from the German Academic Exchange Service (DAAD) for scholarship (No. A/13/92805). The valuable comments of Y.F. Huang are also appreciated.

Author contributions

Y.-C.C. fabricated the samples, performed the experiments, analyzed the data and wrote the manuscript. R.P. and D.G. performed the TEM, EDX, and SAED characterization and analyzed the results. Y.-G.L. conceived and designed XAS characterizations. Y.-K.H. conceived and designed the PEC analyses and interpreted the data. C.F. conceived, designed and supervised the study, interpreted the data and wrote the manuscript. All authors reviewed and approved the manuscript.

Additional information

Supplementary Information accompanies this paper at <https://doi.org/10.1038/s41467-017-02676-w>.

Competing interests: The authors declare no competing financial interests.

Reprints and permission information is available online at <http://npg.nature.com/reprintsandpermissions/>

Publisher's note: Springer Nature remains neutral with regard to jurisdictional claims in published maps and institutional affiliations.



Open Access This article is licensed under a Creative Commons Attribution 4.0 International License, which permits use, sharing, adaptation, distribution and reproduction in any medium or format, as long as you give appropriate credit to the original author(s) and the source, provide a link to the Creative Commons license, and indicate if changes were made. The images or other third party material in this article are included in the article's Creative Commons license, unless indicated otherwise in a credit line to the material. If material is not included in the article's Creative Commons license and your intended use is not permitted by statutory regulation or exceeds the permitted use, you will need to obtain permission directly from the copyright holder. To view a copy of this license, visit <http://creativecommons.org/licenses/by/4.0/>.

© The Author(s) 2018